Hindawi
Geofluids
Volume 2023, Article ID 8890709, 18 pages
https://doi.org/10.1155/2023/8890709

Research Article

Microscopic Pore Structures and Their Controlling Factors of the Lower Carboniferous Luzhai Shale in Guizhong Depression, China

Ren Zhang[1,2], **Shu Jiang**[1,2], **Luchuan Zhang**[1,2], **Hu Wang**[1,2], **Tianyu Zhang**[1,2], **Ruyang Yu**[1,2], **Linhao Zhang**[1,2] and **Finnian Ukaomah Chima**[1,3]

[1]*Key Laboratory of Tectonics and Petroleum Resources, Ministry of Education, China University of Geosciences, Wuhan, Hubei 430074, China*
[2]*School of Earth Resources, China University of Geosciences, Wuhan, Hubei 430074, China*
[3]*Key Laboratory of Continental Shale Hydrocarbon Accumulation and Efficient Development, Ministry of Education, Northeast Petroleum University, Daqing 163318, China*

Correspondence should be addressed to Shu Jiang; jiangsu@cug.edu.cn

Received 16 December 2022; Revised 31 December 2022; Accepted 12 February 2023; Published 13 May 2023

Academic Editor: Mohammed Fattah

Microscopic pore structures are of great significance in evaluating shale gas reservoirs and understanding the occurrence state of shale gas. Integrating geochemical analysis, X-ray diffraction (XRD), low-temperature N_2 adsorption (LTNA), mercury injection pressure (MIP), small-angle X-ray scattering (SAXS), and field emission scanning electron microscope (FE-SEM), this work systematically characterized microscopic pore structures and then discussed their controlling factors, for the Lower Carboniferous Luzhai (C_1lz) shale in Guizhong Depression. The results show that pores in the Luzhai shale are generally shaped by ink bottles, parallel plates, and slits, which are characterized by a larger pore throat ratio, lower efficiency of mercury withdrawal, and poor connectivity. Micropores (<2 nm) and mesopores (2 nm-50 nm) provide the primary specific surface area (SSA) of shale reservoirs, dominantly controlled by the contents of TOC and clay minerals, whereas pore volume is mainly contributed from mesopores, which is positively correlated to quartz content. The fractal dimension (2.94) of macropores is higher than that (2.65) of mesopores, corresponding more complicated and heterogeneous pore structure. With increasing pore size, the correlation between TOC and fractal dimension of macropores weakens. The unconnected pores in mesoscopic range are more complex than connected pores, primarily resulting from morphology and deformation of clay minerals.

1. Introduction

China is rich in shale gas resources, but exploration and development started late, and commercial production is still in the early stage [1–4]. At present, the shale gas enrichment areas that have achieved commercial development are marine shale gas in Sichuan Basin and its surrounding areas, and the shale gas is mainly enriched in the Early Paleozoic Wufeng-Longmaxi Formation [5–9]. Although the production of shale gas in China increased by about 4.66 billion cubic meters in 2020 compared with the previous year [10], the main production gas fields have not changed significantly. Finding shale gas replacement formations and expanding new fields of shale gas exploration and development have become urgent issues for the development of national oil and gas energy. The organic-rich shale is abundant and widely distributed in Guizhong Depression, located in the south of Dian-Qian-Gui area [6, 11]. Its structural deformation and sedimentary characteristics are similar to those of typical shale gas basins in the United States, which has good marine shale gas enrichment conditions. It has been found that the Upper Paleozoic shale gas resources in Guizhong Depression are about 12.34 trillion m^3 [12]. Therefore, Guizhong Depression will probably become

another key exploration area for marine shale gas in southern China after the Sichuan Basin [13, 14]. Many scholars [15–19] have done a lot of research on tectonic evolution, reservoir formation characteristics, preservation conditions, and resource potential of marine shale gas in the Upper Paleozoic in Guizhong Depression and its surrounding areas. However, studies on the precise characterization of reservoir microscopic pores remain scarce.

The pore structure of shale is complex and diverse, and its pore volume and specific surface area play a decisive role in the storage of free gas and adsorption gas, respectively. Therefore, a comprehensive understanding and quantitative characterization of the structural features of shale pores and the main controlling factors are important guidelines for the study of shale gas reservoirs. This can be done via experimental methods which can be divided into three categories [20–22]: (1) image analysis methods like scanning electron microscope (SEM), transmission electron microscope (TEM), atomic force microscopy (AFM), field emission scanning electron microscope (FE-SEM), and other microzone observation technologies which can be used to obtain features of pores, fracture morphology, and other qualitative information in shales [23]; (2) fluid injection technique mainly includes CO_2 adsorption, low-temperature N_2 adsorption (LTNA), CH_4 adsorption, mercury injection pressure (MIP), and water vapor adsorption (WVA), which can quantitatively characterize the pore volume, specific surface area, and pore size distribution at different pore sizes [24]; and (3) nonfluid injection techniques like nuclear magnetic resonance (NMR), small-angle X-ray scattering (SAXS), and micro-nano-CT, which are characterized by simple sample preparation, nondestructive analysis, and strong particle penetration ability and can be combined with other experimental methods to characterize shale reservoirs more accurately [25–27].

Analyzed by MIP and LTNA, organic matter pores, intergranular pores, and microfractures are the main storage space of C_1lz organic-rich shale in Guizhong Depression [28–30]. The pore sizes are mostly in the range of 17 nm~65 nm, with mesopores contributing the most to the shale pore volume, followed by micropores, and the lowest contribution of macropores. Cao et al. [31] found that the influence of different rock layers on shale pore development was not significant and that organic matter abundance and maturity were important factors affecting pore development in shale reservoirs. Li et al. [32] and Zhang and Liu [8] concluded that organic matter- (OM-) hosted pores within bitumen are the primary storage volume, rather than inorganic pores (interparticle and intraparticle) which are rare. Porosity, surface areas, and pore volumes exhibit positive correlations with TOC (total organic carbon), R_o (vitrinite reflectance), and siliceous mineral contents. However, previous studies of shale pores have certain limitations, such as the relatively large diameter of mercury molecules and their nonwetting nature, which cannot fully enter the pores and throats less than 3 nm in diameter at 413 MPa. Although the nitrogen molecules are small in diameter and can start adsorption from the pore surface, they cannot enter the closed pores, while the penetration of small-angle X-rays is an important means of exploring the complementary formation of closed pore information (Figure 1). In this study, we will (a) combine FE-SEM, MIP, LTNA, and SAXS to qualitatively and quantitatively characterize the pore structure and pore size distribution of shale and their primary control factors and (b) discuss the mineralogical control factors for both connected and unconnected pore features and complexity at different scales, which may conduce to the prediction of sweet spots.

2. Geological Setting

Guizhong Depression is a secondary tectonic unit in the northeast of the Dian-Qian-Gui oil-gas-bearing area (Figure 2A), located in the combination of the southwest margin of the Yangtze block and the South China Caledonian fold belt. It is a large marine residual depression based on the Caledonian Movement in the Late Paleozoic [15, 34–36]. The formation and evolution of Guizhong Depression can be divided into four stages: (1) the formation of the crystalline basement of the depression, (2) early proto-Tethys rifting into basins and late fold orogeny, (3) the Paleo-Tethys rift forming the basin again, and (4) the neo-Tethys orogeny reforming. According to the characteristics of combination of the tectonic deformation and the location of deep major faults, the study area can be divided into eight subtectonic units, i.e., Huanjiang shallow depression, Yishan fault depression, Hongdu shallow depression, Xiangzhou shallow depression, Masan fault ridge, Luocheng low relief, Liucheng low relief, and Liucheng slope [36, 37] (Figure 2B. NNE-NE and E-W deep-large faults are mainly developed in the study area, most of which have strike-slip and high-angle thrust properties. Since Early Devonian, intraplate rifting activity caused the study area to sink into a basin and began to receive marine deposits. Later, the inland expansion from the late Early Devonian to the Early Carboniferous formed a platform and basin alternate passive continental marginal basin pattern [15, 37].

The shale of C_1lz is widely distributed in the study area, with high organic matter content and thicknesses of 50 m-500 m; lithology mainly includes carbonaceous mudstone, shale, and silty mudstone [12] (Figure 2C). Under the influence of Yanshan and Himalayan movements, the Carboniferous and caprocks suffered denudation in the north and east of the region [38]. However, the organic-rich shales of C_1lz are still relatively intact in most of the syncline cores, and the depth of burial is mostly less than 2800 m, which has great potential for exploration and development.

3. Sample and Method

3.1. Sample Collection and Analyses. In this paper, 19 samples were collected and analyzed from C_1lz in Well GRY-1 (7), Well GLD-1 (3), outcrop PM-A (4), and PM-B (5) in Guizhong Depression (Figure 2C). The experimental results are shown in Table 1. The Luzhai Formation shale has high organic matter abundance; the total organic content (TOC) varies from 0.69% to 2.23%, with a mean of 1.39%; thermal maturity R_o ranges from 2.05% to 2.87%, with an average of 2.45% (Table 1).

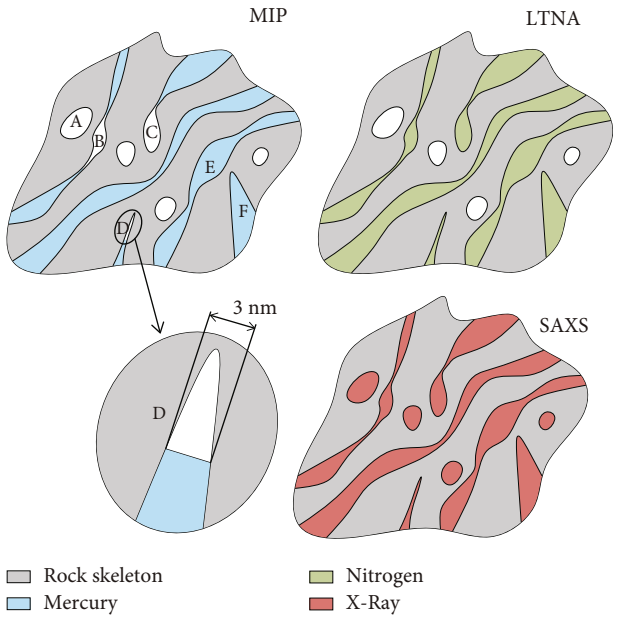

Figure 1: Types of shale pore structure and pore space accessible by different testing methods [33]. A Closed. B, E Passing. C, D, F Dead end.

The D8 ADVANCE X-ray diffractometer of Bruker AXS company was used to determine the mineral composition of the samples. The main content of minerals is quartz, ranging from 40.00% to 59.5%, with an average of 45.24%, followed by clay minerals, ranging from 10.7% to 42.7%, with an average of 26.7% (Table 1). In addition, the samples also contain smaller amounts of calcite, dolomite, feldspar, and pyrite.

3.2. Experimental Method

3.2.1. Field Emission Scanning Electron Microscopy (FE-SEM). The morphology of shale sample was observed by FE-SEM (JSM-6610LV) with the acceleration voltage of 20 kV. The sample was cut into a one-centimeter square, with a thickness of 0.5 cm, which was polished by argon ion, and plated with a layer of 10 nm-20 nm thick platinum film on the sample surface. Then, the prepared shale samples were tested under an accelerating voltage of 2 kV, with a resolution of 4 nm. The experiment was completed at a temperature of 30°C and a humidity of 20%.

3.2.2. Mercury Intrusion Porosimetry. The MIP was completed with a Micromeritics AutoPore V9620 high-pressure mercury intrusion instrument. The sample was a 2 g cube with a side length of 1 cm, the surface was polished (to reduce the hemp skin effect), and it was dried at 60°C for more than 48 hours until the weight did not change. The mercury injection pressure was increased from 5 psia (0.034 MPa) to 60000 psia (413 MPa), mercury surface tension was 0.485 N/m, and the contact angle was 130°. Pore sizes, volumes, and surface areas were calculated by the Washburn and Young-Dupré equation [41, 42].

3.2.3. Low-Temperature N_2 Adsorption. Low-temperature N_2 adsorption was carried out at -196.15°C using an ASAP 2460 pore size analyzer apparatus made by McMerritik (Shanghai) Instrument Co., Ltd. Before measurement, samples were crushed into a 60-80 mesh particle and undergo vacuum degassing treatment to remove adsorbed moisture and volatile matter at 110°C for more than 24 h. In the adsorption and desorption experiments, the relative pressure ranged from 0.005 to 0.995, with a constant temperature of 77.35 K, and the equilibrium interval was 30 s. The pore size distribution and specific surface area were calculated according to the Barrett-Joyner-Halenda (BJH) equation and the BET equation, respectively.

3.2.4. Small-Angle X-Ray Scattering (SAXS). This experiment was conducted by the Mar165 CCD detector of research at Shanghai Synchrotron Radiation Light Source Small-Angle Scattering Station, using neutron wavelengths of $\lambda = 1.54$ Å , and the distance from the sample to the detector was 1850 mm. Each sample was cut into a square with a side length of 1 mm along the bedding direction, and the thickness is controlled at 0.8 mm to prevent multiple scattering. After sample preparation, the samples were placed in an oven at 60°C for more than 24 hours to remove the influence of hydrogen-containing substances in samples on the experiment. The scattered intensity plane distribution recorded by the 2D detector was one dimensionalization, and the background was corrected by the sector integration method to obtain the final shale sample structure information [43, 44].

4. Results

4.1. Observation of FE-SEM. According to the location of pores and their relationship with rock grains, shale pore types were divided into three categories: organic pores, mineral matrix pores, and fracture pores. Mineral matrix pores can be further divided into intergranular pores and intragranular pores [45–47]. The organic matter pores between 5 and 500 nm are mostly flat, irregular, or round, with smooth and well-defined pore edges (Figures 3(a) and 3(b)). Granular pyrite agglomerates are usually filled with organic matter, due to the stronger support between the rigid mineral particles; the intervening organic matter pores are less affected by late compaction [46] and are mostly circular (Figure 3(c)). The intergranular pores are mainly formed by the mutual support of rigid minerals such as pyrite, calcite, and quartz, which are triangular, elongated, and irregular. The pore edge is flat, and the pore diameter is more than several hundred nanometers (Figures 3(d)–3(f)). With the increase of burial depth, compaction and cement filling leads to a continuous decrease in intergranular pore size [48]. Due to the resulting shrinkage of organic matter, the volume of organic matter decreases, resulting in the formation of pyrite cavities between minerals and organic matter (Figure 3(g)). The size of these cavities is micro- and nanometer ranges from a few microns to a few nanometers, with good connectivity to organic matter pores, forming a good storage and percolation network. Intragranular pores are mainly developed in mineral aggregates with relatively well-crystal shapes and

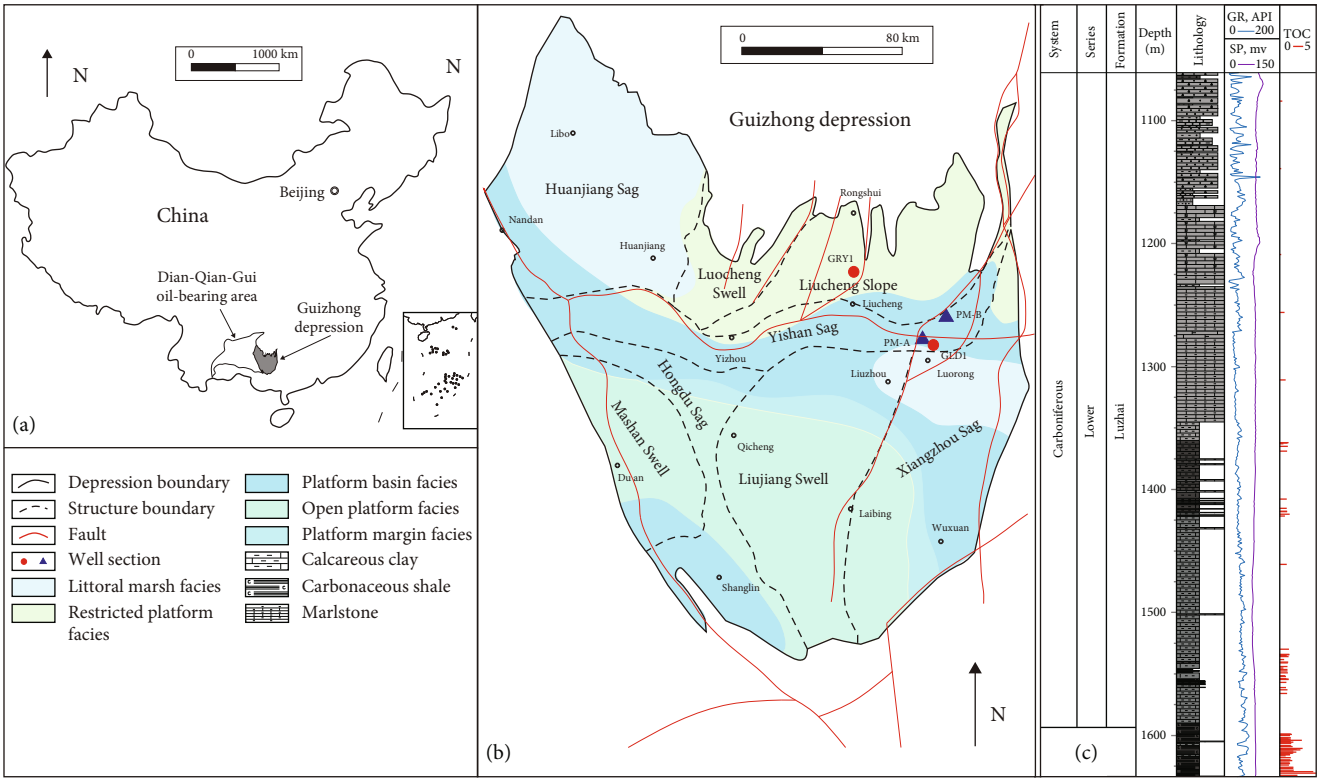

Figure 2: Structure division and stratigraphic column of the Guizhong Depression [11, 39, 40]. (a) The map of China. (b) Structure division of the Guizhong Depression. (c) Stratigraphic column of Luzhai Formation.

Table 1: Basic compositions of the C_1lz shale sample.

Sample ID	Quantitative analysis of whole-rock minerals (wt%)							TOC (%)	R_o (%)
	Quartz	K-feldspar	Plagioclase	Calcite	Dolomite	Pyrite	Clay		
GRY-1	40.20	0.00	0.00	32.40	5.40	3.10	18.90	1.09	2.62
GRY-2	45.80	0.00	1.10	21.90	5.70	2.70	22.80	0.69	2.65
GRY-3	45.00	0.00	0.90	9.60	19.70	3.30	21.50	1.20	2.67
GRY-4	/	/	/	/	/	/	/	0.86	2.69
GRY-5	55.00	0.00	1.40	1.00	1.80	0.00	40.80	1.50	2.66
GRY-6	/	/	/	/	/	/	/	2.23	2.84
GRY-7	45.00	0.00	0.00	17.00	0.00	3.00	35.00	1.39	2.87
GLD-1	43.60	2.00	3.70	3.40	3.60	4.70	39.00	1.05	2.22
GLD-2	49.90	1.70	6.70	5.00	14.80	7.20	14.70	1.03	2.24
GLD-3	40.00	0.30	2.90	1.40	29.20	5.70	20.50	1.02	2.30
PM-A1	59.50	0.00	12.50	0.00	2.70	0.00	25.30	1.97	2.05
PM-A2	55.00	0.00	2.00	3.00	2.50	7.00	30.50	/	/
PM-A3	55.10	0.00	1.50	0.70	0.00	0.00	42.70	1.20	/
PM-A4	45.00	0.00	4.20	40.10	0.00	0.00	10.70	0.71	/
PM-B1	45.00	0.00	4.20	29.20	0.00	5.70	15.90	1.47	/
PM-B2	50.00	0.80	1.00	10.40	5.80	6.10	25.90	1.80	2.25
PM-B3	54.90	0.00	7.80	0.00	5.50	3.50	28.30	2.20	2.19
PM-B4	53.50	0.90	5.10	0.00	0.00	4.60	35.90	2.04	2.31
PM-B5	58.90	0.00	1.00	0.00	0.00	0.60	39.50	1.60	/

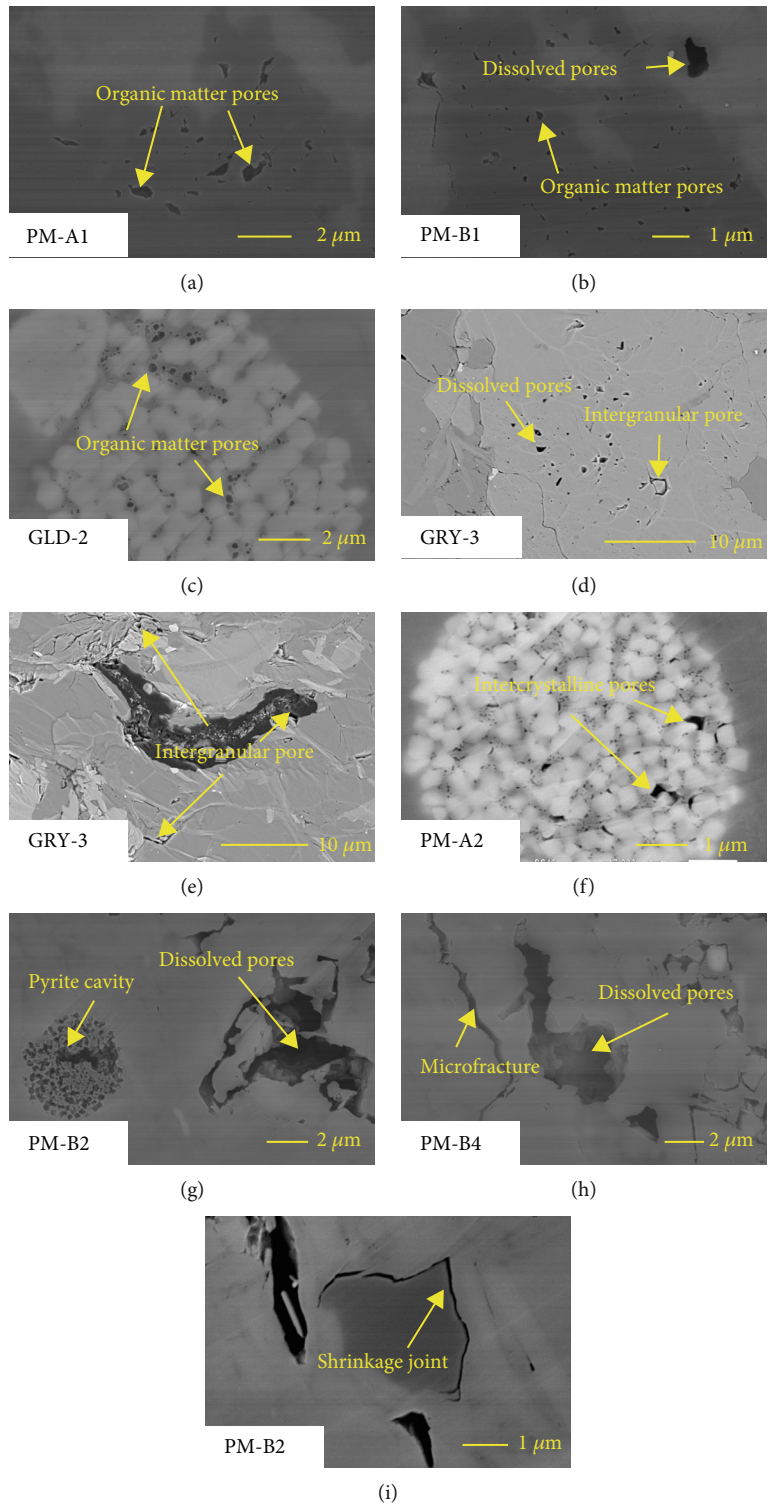

Figure 3: SEM images of shale samples from the C_1lz in the Guizhong Depression.

coarse crystals such as pyrite, quartz, calcite, and clay (Figure 3(f)). They are mostly caused by lattice defects during diagenesis, and their widths are generally tens of nanometers, but the length generally extends longer. Intragranular dissolved pores are mainly developed in calcite, feldspar, and other soluble mineral particles. The pores are always circular, elliptical, and irregular, and the pore size is generally nanoscale, with larger pores occurring up to several micrometers in size [49] (Figures 3(g) and 3(h)). Fracture pores are mostly formed by the action of geological tectonic stress and generally have obvious directionality with long extensions, most of which are linear or folded (Figure 3(h)). They cross-bred different rock components and form intersecting beds at different oblique angles. When

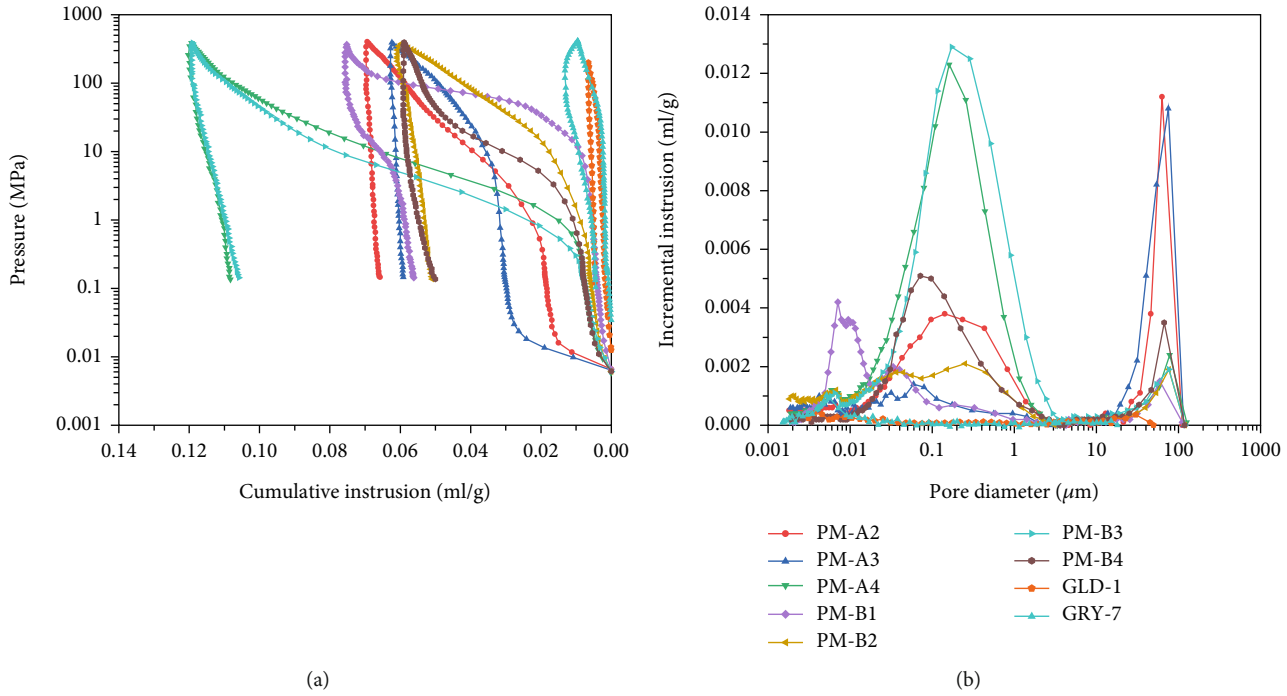

Figure 4: Mercury injection curve and pore throat distribution curve.

organic matter in contact with the massive minerals undergoes polycondensation and consolidation, organic matter shrinkage joint is easily generated (Figure 3(i)). Such cracks generally do not extend far, which is conducive to improving the porosity and permeability conditions of shale. Such fractures play a significant role in promoting the later fracturing transformation within the shale reservoir.

4.2. Shale Pore Features

4.2.1. MIP. The shape of the mercury injection curve can reflect the throat distribution and the connectivity [50]. It can be seen from Figure 4(a) that the displacement pressure for the samples is about 0.01 MPa. With the increase of capillary force, the curve presents two different morphological characteristics (Figure 4(a)). These are categorized into type I samples (PM-A2 and PM-A3) which are characterized by rapid increase in cumulative intrusion to 0.02 ml/g followed by a slow and then rapid increase after displacement pressure is attained. For the rest samples of type II, the cumulative intrusion increased slowly after reaching the displacement pressure, but when the pressure reaches 1 MPa, it experiences a rapid increase and finally reaches the saturation state slowly. The mercury injection curve of type I samples is inverse S-shaped as a whole, with two near-horizontal sections, indicating that the throat sorting is poor and the pore throats are not uniformly developed. The curves of the type II samples are at the upper right, and the near-horizontal section is significantly longer than that of the type I, indicating that it has good sorting and large proportion of pore throat.

The pore diameter distribution curve is bimodal (Figure 4(b)), and the peaks of the curve appear at 0.2 μm-0.3 μm and 50 μm-60 μm, respectively. There are differences in the pore throat radius of the main peak between different samples. Type I samples are postpeak type, dominated by medium throat. Type II samples are prepeak type, dominated by thin throats. The pore volume is in the range of 0.00418 cm^3/g-0.05975 cm^3/g, with an average of 0.02142 cm^3/g. The specific surface area is in the range of 1.35 m^2/g-15 m^2/g, on average 6.62 m^2/g. The average pore size is 9.82 nm-42.9 nm, with an average of 19.90 nm. The porosity of MIP is 0.95%-2.40%, with an average of 1.21%. The efficiency of mercury withdrawal is 5.0%-53.6%, with an average of 18.3% (Table 2); the low efficiency of mercury withdrawal indicates a large pore throat ratio and poor pore connectivity. Tectonic movements caused the shale to be lifted to the surface and suffer weathering and scouring, so its porosity, pore volume, and specific surface area are significantly higher than those of core samples.

4.2.2. LTNA. During the low-temperature nitrogen adsorption test, nitrogen molecules carry out monolayer adsorption, multilayer adsorption, and capillary condensation on the pore surface during the increase of relative pressure. As relative pressure decreases, the nitrogen molecules adsorbed on the surface of shale pores began to desorb, but the adsorption and desorption curves do not overlap at the same pressure. The shape of the hysteresis loop in the middle of the two curves can explain the morphological characteristics of the pores to some extent [51–53]. According to the IUPAC classification scheme [52, 54], the adsorption-desorption curves of shale samples in the study area can be divided into two types: H2 and H3 (Figure 5(a)). The H2-type desorption curve is almost

Table 2: Parameters of shale pore structure obtained by high-pressure mercury intrusion, nitrogen adsorption, and small-angle scattering.

Sample ID	MIP				LTNA			SAXS		
	Pore volume (10^{-3} cm^3/g)	SSA (m^2/g)	Average pore diameter (nm)	Efficiency of mercury withdrawal (%)	BJH pore volume (10^{-3} cm^3/g)	BET SSA (m^2/g)	Average pore diameter (nm)	Pore volume (10^{-3} cm^3/cm^3)	SSA (m^2/g)	Average pore diameter (nm)
GRY-1	4.18	1.59	10.51	57	20.66	8.64	11.63	13.73	9.28	17.73
GRY-2	5.05	2.01	10.04	58	14.30	7.48	10.11	13.32	8.55	18.48
GRY-3	7.17	1.76	16.27	37	23.02	12.86	8.96	20.50	13.41	18.84
GRY-4	4.60	1.35	13.60	33	16.61	5.36	14.67	10.59	7.26	17.07
GRY-5	7.77	3.17	9.82	53	29.74	16.47	9.28	13.10	9.86	16.13
GRY-6	7.68	2.51	12.23	44	23.05	17.24	6.94	20.87	14.89	18.09
GRY-7	9.60	3.23	11.91	54	22.39	11.38	12.63	18.22	12.75	17.99
GLD-1	6.54	/	29.70	28	7.9	4.08	12.10	/	/	/
GLD-2	7.16	/	32.00	29	8.2	6.01	9.87	/	/	/
GLD-3	6.14	/	42.90	20	5.2	4.86	9.30	/	/	/
PM-C1	37.75	15.00	/	26	47.09	22.65	8.32	/	/	/
PM-C2	30.35	14.36	/	17	29.37	20.66	5.69	/	/	/
PM-C3	59.50	8.49	/	12	42.51	15.97	10.65	/	/	/
PM-C4	29.50	5.25	/	15	22.99	9.41	9.77	/	/	/
PM-C5	30.85	7.33	/	9	22.73	14.72	6.18	/	/	/
PM-B1	27.25	10.40	/	19	23.38	21.86	4.28	/	/	/
PM-B2	34.75	8.67	/	5	22.59	14.80	6.10	/	/	/
PM-B3	31.40	9.78	/	6	20.56	16.71	4.92	/	/	/
PM-B4	59.75	11.08	/	10	36.57	16.59	8.82	/	/	/

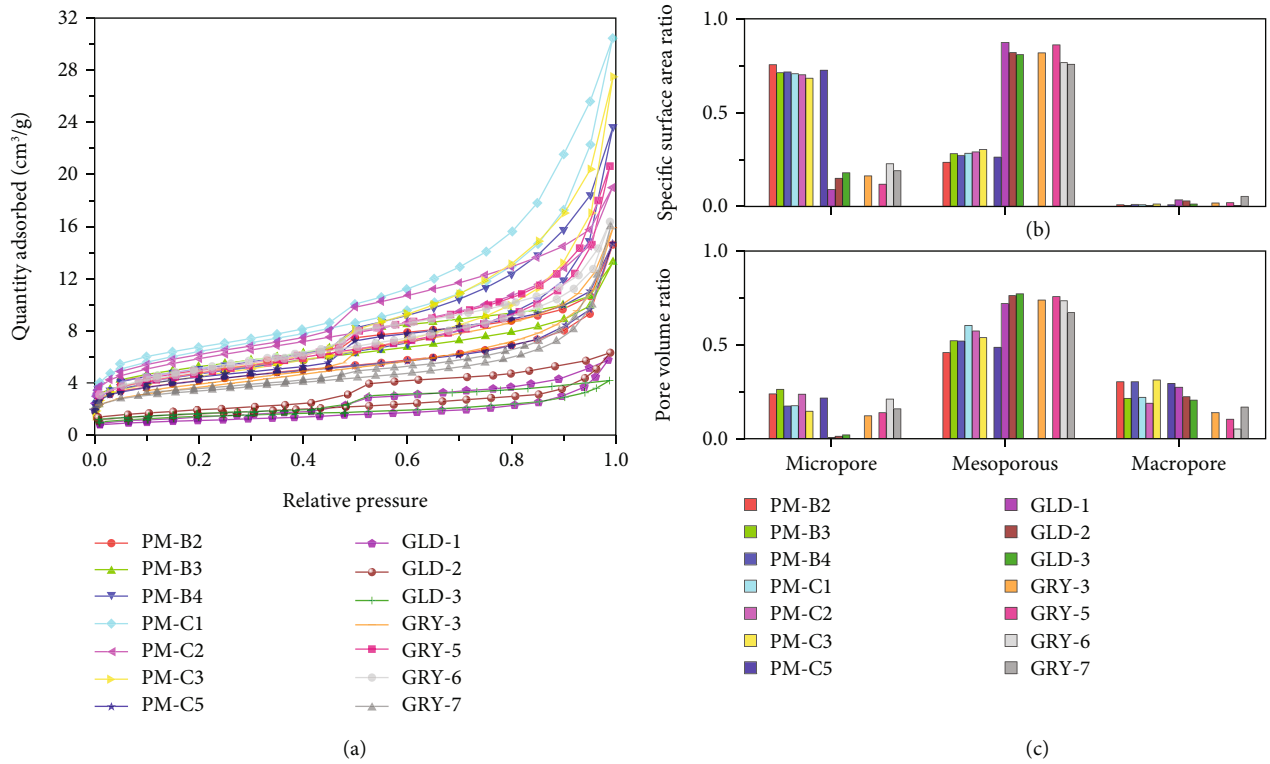

Figure 5: Nitrogen adsorption curve and pore size distribution histogram.

horizontal in the part of $P/P_0 > 0.5$, while it coincides with the adsorption curve when $P/P_0 < 0.5$ (GLD-1, GLD-2, and GLD-3), reflecting a large number of ink bottle-type pores in the shale. The remaining samples mainly exhibit the characteristics of the H3 type, and the desorption curve decreases gradually with the decrease of P/P_0 until it overlaps with the adsorption curve, reflecting that the shale is mainly developed with parallel plates and fracture-like pores.

The BJH pore volume was 0.00520 cm^3/g-0.04709 cm^3/g, with an average of 0.02310 cm^3/g. The BET-specific surface area was 4.08 m^2/g-22.65m^2/g, with an average of 13.04 m^2/g (Table 2). Figures 5(b) and 5(c) show the pore volume and specific surface area distributions of the shale samples from the study area. The pore volume was dominated by the contribution of mesopores, accounting for 50%-80%, and the proportion of micropores and macropores was equal. The specific surface area of the outcrop samples was dominated by the contribution of micropores, followed by mesopores. The contribution rate of mesopore to the specific surface area of core samples is up to 80%, followed by micropore.

4.2.3. SAXS. Small-angle X-ray scattering (SAXS) is one of the main methods for studying the structure of matter at the nanoscale. X-rays can penetrate the sample and obtain all the structural information of the connected and unconnected pores [55, 56] (Figure 1). Figure 6(a) shows the method of one-dimensionalization of the planar distribution of the small-angle scattering intensity by means of sector integration. Figure 6(b) shows the original data curve of the shale sample measured by small-angle scattering and the curve after deducting the scattering background. The small-angle X-ray scattering curve of the shale sample was fitted by the non-negative least square method. Then, the porosity, pore number density (number of pores per unit volume), and pore size distribution were obtained by the polydispersed pore size distribution model [57]. Affected by the distance from the sample to the detector, the pore size characterized by this small-angle X-ray scattering experiment ranged from 3 nm to 40 nm. The pore volume is in the range of 0.01310 cm^3/g-0.02087 cm^3/g, with an average of 0.01576 cm^3/g. The specific surface area is in the range of 7.26 m^2/g-14.89 m^2/g, with an average 10.86 m^2/g. The average pore size is 16.13 nm-18.84 nm, with an average of 17.76 nm.

4.3. Fractal Characteristics. Fractal geometry was first proposed by Mandelbrot et al. [59] and applied to the study of shale pore characteristics. Different from the classical Euclidean dimension theory, fractal theory has more advantages in describing the roughness and complexity of pores in porous media such as tight oil and gas, shale, and coal reservoirs [60, 61]. The fractal dimension of pores is a fraction between 2 and 3: the closer to 2, the smoother the pore surface and the less heterogeneity; the closer to 3, the rougher the pore surface becomes and the more heterogeneity. Figure 7 shows the fractal features of three different characterization methods using the A5 sample as an example.

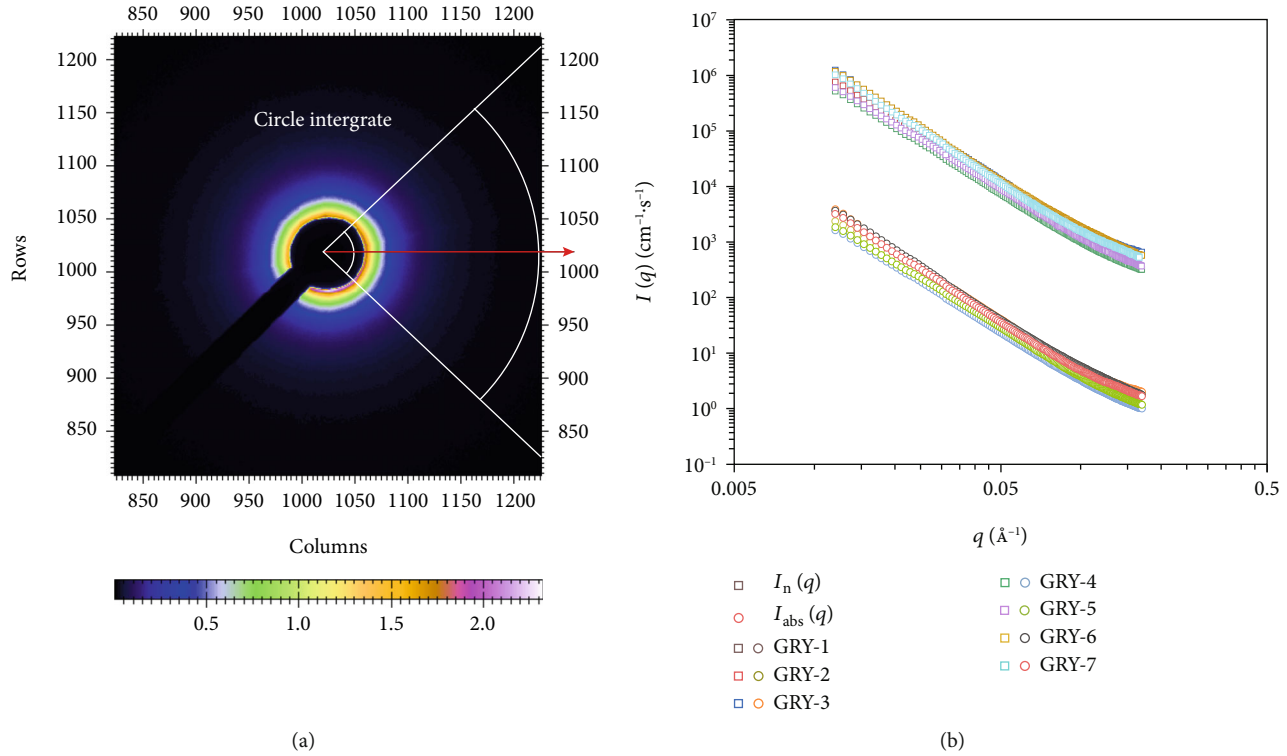

FIGURE 6: (a) Schematic diagram of small-angle X-ray fan integral [58]. (b) One-dimensional plotted scattering intensity and background-subtracted intensity.

MIP (Figure 7(a)). Based on the geometric principle of fractal, the fractal dimension D can be calculated by bringing the experimental data of MIP into [62]

$$\mathrm{Log}\left(1 - S_g\right) = (D-3)\,\mathrm{Log}\,P_c - (D-3)\,\mathrm{Log}\,P_{\min}, \quad (1)$$

where S_g is the saturation of the wetting phase fluid (%), P_c is the capillary force corresponding to the saturation S_g, and $P_{\min}$ is the capillary force corresponding to the maximum pore throat radius.

LTNA (Figure 7(b)). According to the FHH equation (2) [59] and the experimental data, $\ln(V)$ changes linearly with $\ln(\ln(P_0/P))$, and the slope is the fractal dimension D of the shale sample.

$$\ln(V) = (D-3)\ \ln\ (\ln(P_0/P)) + C, \quad (2)$$

where V is the nitrogen adsorption amount under the condition of equilibrium pressure P, P_0 is the saturation pressure, C is a constant, and D is the fractal dimension. By the Kelvin equation $r_k = -0.414/(\lg P/P_0)$, the radius of curvature of the adsorbed gas condensed in the pores can be calculated. Then, use the Haley equation $t = 0.354[-5/\ln(P/P_0)]^{1/3}$, and calculate the liquid film thickness t. Finally, for the cylindrical hole, its radius can be obtained by adding the calculated film thickness and curvature radius: $r_p = r_k + t$, so the corresponding relationship between the pore radius and P/P_0 can be obtained [63]. Combined with equation (2), the fractal dimension of pores in the corresponding pore size range is obtained.

SAXS (Figure 7(c)). The SAXS curve generated by the fractal follows an exponential law, $I(q) \propto q^{-\alpha}$. $-\alpha$ is the slope of the $\ln I(q) - \mathrm{lnq}$ curve in the linear region, and if α is between 0 and 4, it indicates the existence of fractal phenomena [56]. When $3 \le \alpha < 4$, it indicates that the shale pores have surface fractal characteristics, and $D_s = 6 - \alpha$. If D_s is close to 2, the pore surface is smoother; otherwise, the pore surface is rougher. When $0 < \alpha < 3$, it indicates the existence of mass fractal or hole fractal, and $D_m = \alpha$ or $D_p = \alpha$ [26].

Table 3 summarizes the fractal dimensions of the seven shale samples in the study area measured by three methods. For MIP, when the pore size is less than 50 nm, the fractal dimension D_{m1} of shale samples is mostly less than 2, indicating that the fractal characteristics of shale pores are not obvious in this range. For the part from 50 nm to 5 μm, the average fractal dimension D_{m2} is 2.96, and R^2 is 0.99; for the part larger than 5 μm, the average fractal dimension D_{m3} is 2.94, and R^2 is 0.99 too. At the macropore scale, the accessible pore structure of shale is complex, the pore surface is rough, and the fractal characteristics are obvious. The average fractal dimension in the range of 4 nm-50 nm measured by LTNA is 2.65, and the variance is 0.001155. The average fractal dimension in the range of 4 nm-50 nm measured by SAXS is 2.87, and the variance is 0.0027633. Because small-angle scattering is the detection of all pores

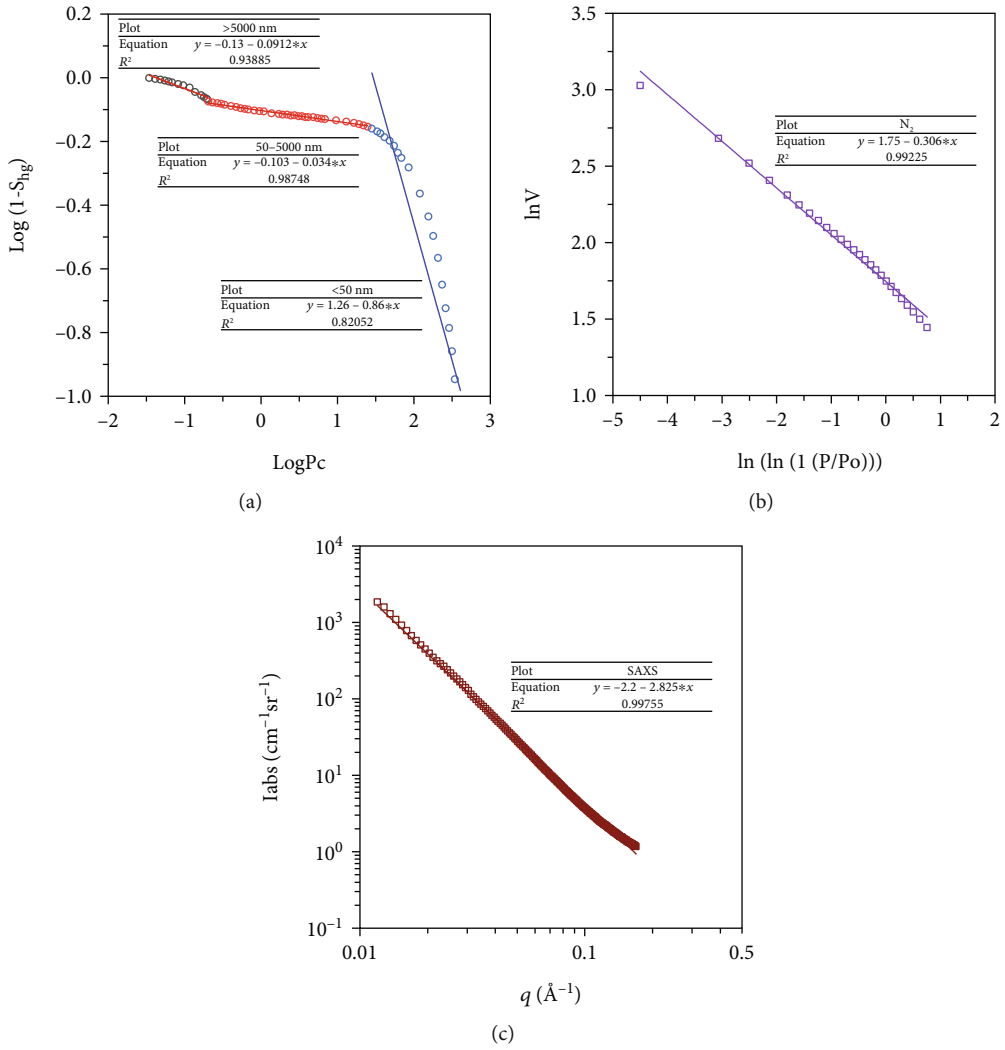

Figure 7: Fractal dimension fitting of MIP (a), LTNA (b), and SAXS (c).

Table 3: Statistics of pore fractal dimension.

Sample ID	Fractal dimension				
	MIP			LTNA	SAXS
	D_{m1} (<50 nm)	D_{m2} (50 nm-5 μm)	D_{m3} (>5 μm)	D_N (2 nm-50 nm)	D_S (2 nm-50 nm)
GRY-1	2.11	2.98	2.97	2.67	2.93
GRY-2	1.84	2.96	2.92	2.69	2.95
GRY-3	1.34	2.95	2.95	2.70	2.84
GRY-4	1.59	2.96	2.93	2.61	2.82
GRY-5	2.14	2.97	2.99	2.69	2.83
GRY-6	1.96	2.91	2.90	2.74	2.86
GRY-7	1.79	2.96	2.93	2.71	2.85

in shale (including unconnected pores), the complex difference between connected and unconnected pores can be inferred by comparing with the difference of fractal dimensions measured by LTNA and SAXS [64]. The fractal dimension and its variance measured by the small-angle scattering method are significantly higher than those measured by the liquid nitrogen method, indicating that the pore structure of unconnected pores is more complex than that of connected pores. It is more conducive to the adsorption of shale gas, and communicating as many unconnected pores as possible in the production process will significantly increase shale gas production.

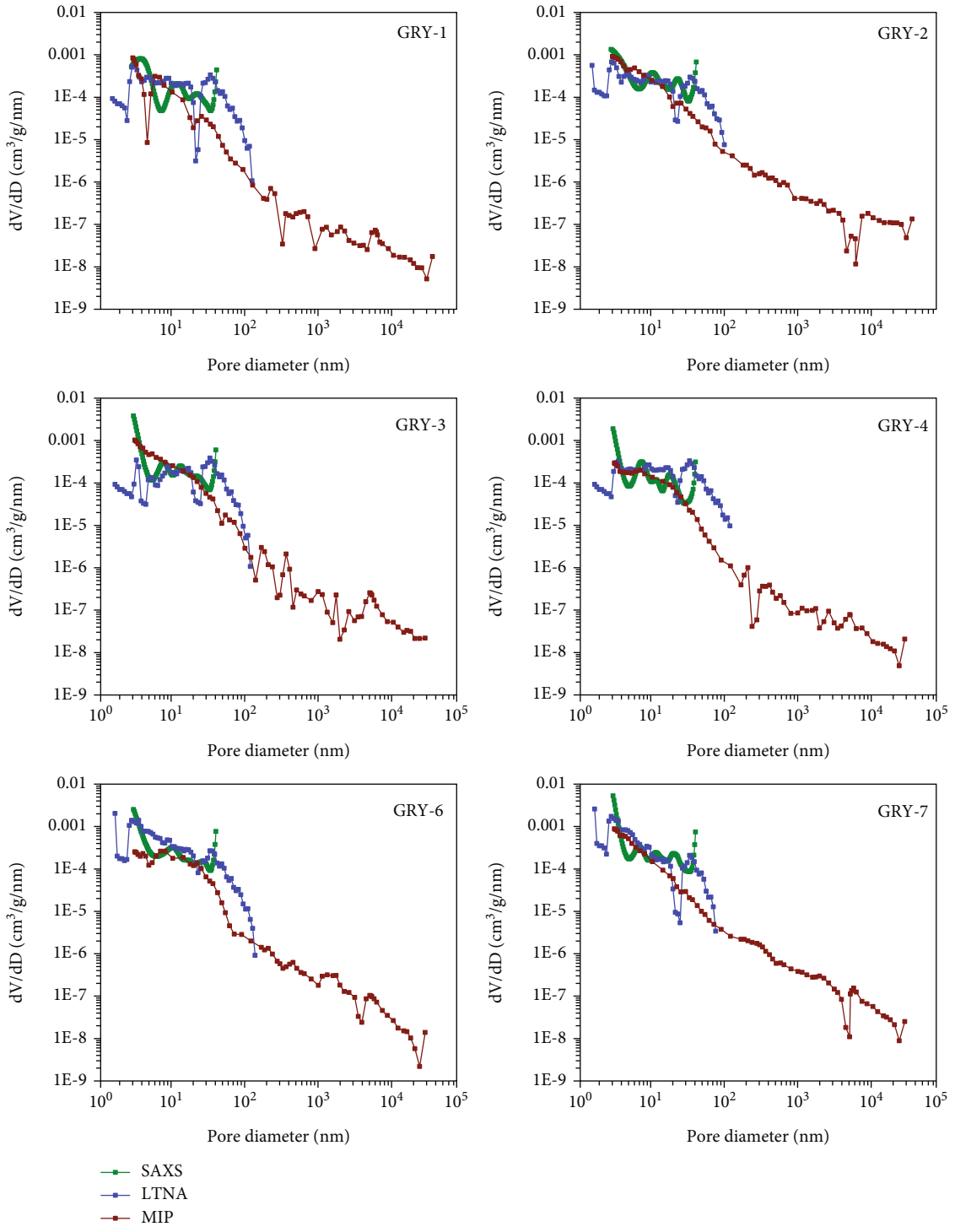

Figure 8: Pore volume distributions with pore sizes from SAXS and LTNA as well as pore throat sizes from MICP, for six shale samples.

5. Discussion

5.1. PSD Analysis. The measurement results of LTNA, MIP, and SAXS on the pore size distribution of shale samples are shown in Figure 8. The pore size distribution curves of MIP are below the other two curves. Because the mercury molecules are nonwettable to shale and cannot fully enter the relatively small connected and unconnected pores, the measured value is smaller relatively. The MIP pore size distribution curve is obviously higher than other curves in the 8 nm pore size range, the main reason may be that the shale samples develop a large number of ink bottle-type pores with this throat diameter. The pore size distribution curve of LTNA is slightly higher than that of

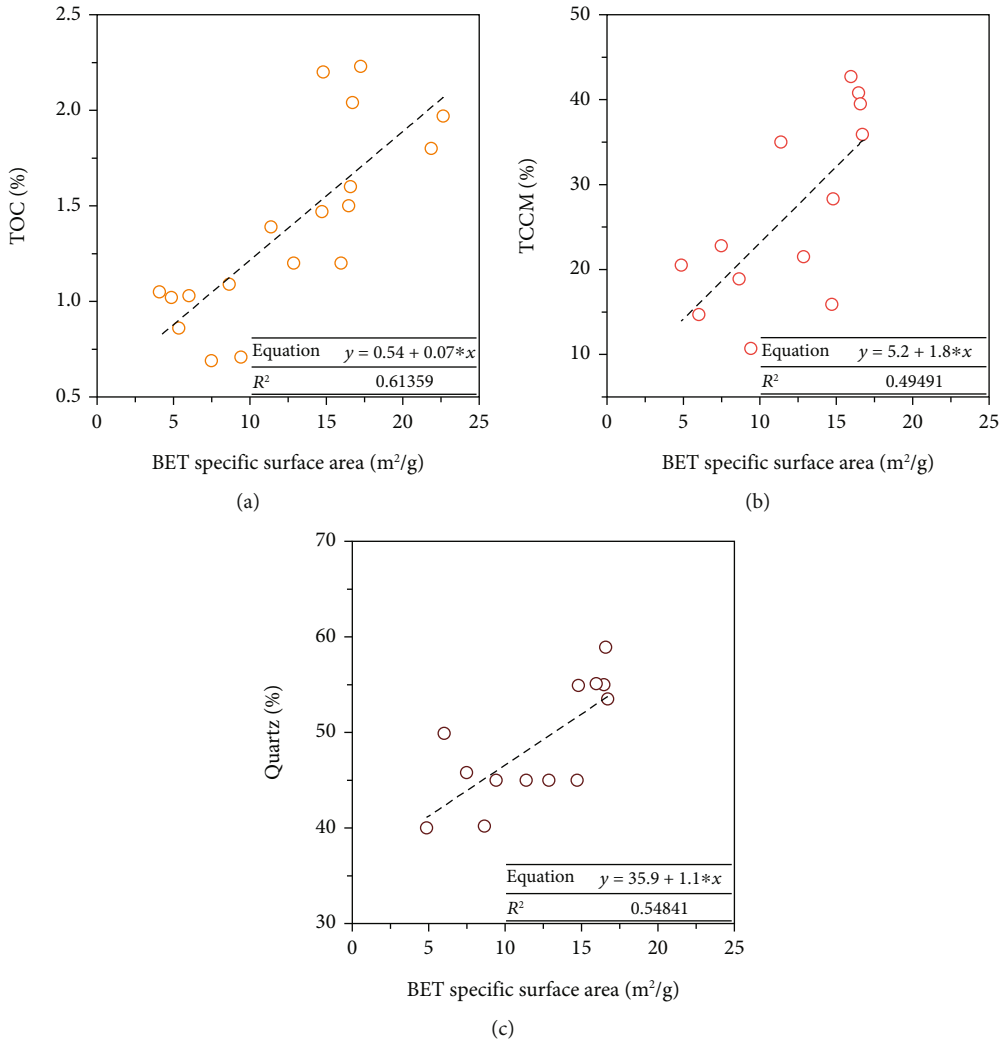

Figure 9: BET-specific surface area correlation analysis.

the other two curves on the whole. The main reason is that the sample used for LTNA is powder, and some small throats and obturator pores are damaged in the sample preparation process, resulting in a large measured value. According to the pore size distribution curve of SAXS, as the pore size increases, dV/dD decreases and then increases in general, with a peak at each end of the curve. Based on the pore size distribution curve, with the increase in pore size, dV/dD shows a change characteristic of first increasing and then decreasing, and there is a peak at each end of the curve (Figure 8), indicating that pore develops better in the pore size less than 3 nm and larger than 40 nm. The interior of the interval shows multiple peaks, but low values and the pore size distribution are relatively uniform. From the characteristics of the end of the SAXS curve, under the same pore size, the pore size distribution measured by SAXS has an upward trend, while the MIP and LTNA layers have an obvious downward trend, indicating that there are many unconnected pores development at the pore size larger than 40 nm and smaller than 3 nm.

5.2. Key Factors Controlling Nanopore Systems. Based on LTNA data, a correlation analysis of shale pore characteristics is made (Figure 9). The BET-specific surface area is positively correlated with TOC, TCCM (total content of clay minerals), and quartz content; R^2 are 0.61, 0.49, and 0.57, respectively. Large numbers of organic matter pores were generated during the generation and emission process of hydrocarbon, which provided a large amount of specific surface area for the shale. The correlation factor R^2 between specific surface area and TOC is much lower than that of Wufeng-Longmaxi Formation (average 0.9 [65]). The main reason is that the TOC of the study area is much lower than that of the Wufeng-Longmaxi Formation (average 4.46%), and the level of organic matter pore development is relatively low. Clay minerals can provide a certain specific surface area, but their contribution capacity is much lower than that of organic matter due to the difference in pore size scale and pore surface morphology, showing a relatively low correlation between specific surface area and clay mineral content [66]. The high correlation with quartz content may be attributed to the high content of biosilicon in shale of

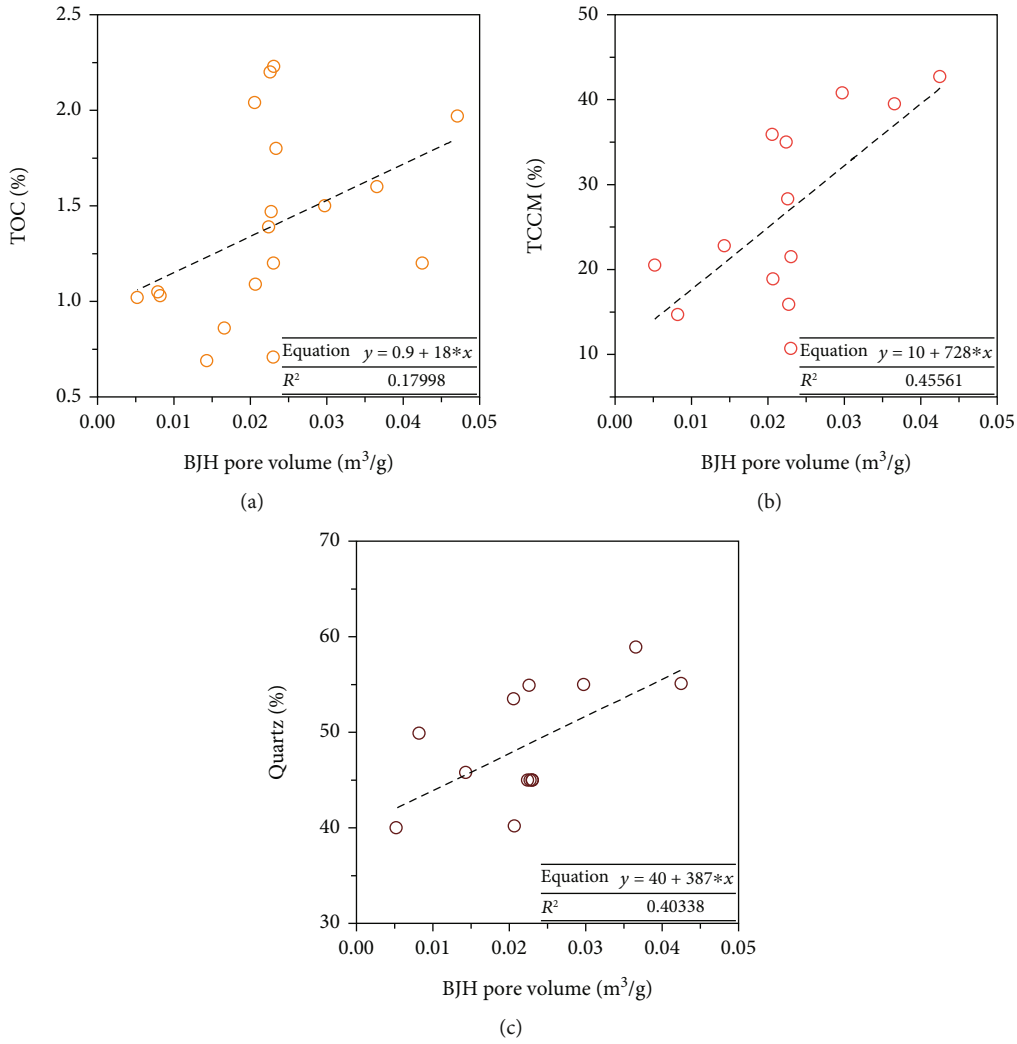

Figure 10: BJH pore volume correlation analysis.

C_1lz. The inner structure of silicon-rich plankton dissolves preferentially than the siliceous shells; then, the siliceous shell opal A transformed into a crystalline structure of high hardness [67]. The internal pores of silicon-rich plankton are preserved, and their average diameter is typically 5-10 nm, which is one of the major contributors to BET-specific surface area.

The BJH pore volume is positively correlated with the clay and quartz contents (Figure 10); R^2 are 0.46 and 0.40, respectively. With the increase of quartz and clay contents, the pore volume of BJH showed an obvious increasing trend. During the whole process of hydrocarbon source rock evolution, with the increasing degree of thermal evolution, montmorillonite and kaolinite in clay minerals gradually transformed to illite, and the interlayer water detachment led to the formation of a large number of pores. The high degree of thermal evolution (R_o average 2.45%) of organic-rich shales in the C_1lz of the Guizhong Depression is an important reason for the good correlation between shale clay mineral content and pore volume in the study area. In terms of microscopic characteristics, biosilicon is mostly produced as chain-shaped microcrystalline quartz or its aggregates [68, 69]. These microcrystalline quartz particles serve as the rock support framework and develop a large number of intergranular pores and dissolution pores. Such related pores are an important contributor to BJH pore volume.

The average pore size is negatively correlated with TOC, and there is no obvious correlation with quartz and clay (Figure 11). The organic-rich shale of the Luzhai Formation in the study area has a high degree of thermal evolution, and with the increase in burial depth, under the strong tectonic activity, the organic pores gradually collapsed and flattened, resulting in a great change in the structure and a decrease in the diameter of the pore throat. Similar to the high-maturity organic-rich shale in the Wufeng-Longmaxi Formation, with the increase of depth and maturity, the correlation of average pore size and TOC changed from positive to negative.

5.3. Influencing Factors of Fractal Dimension. When the pore size of the shale is larger than 50 nm, the fractal dimension D_{m2} of mercury injection has a strong negative correlation

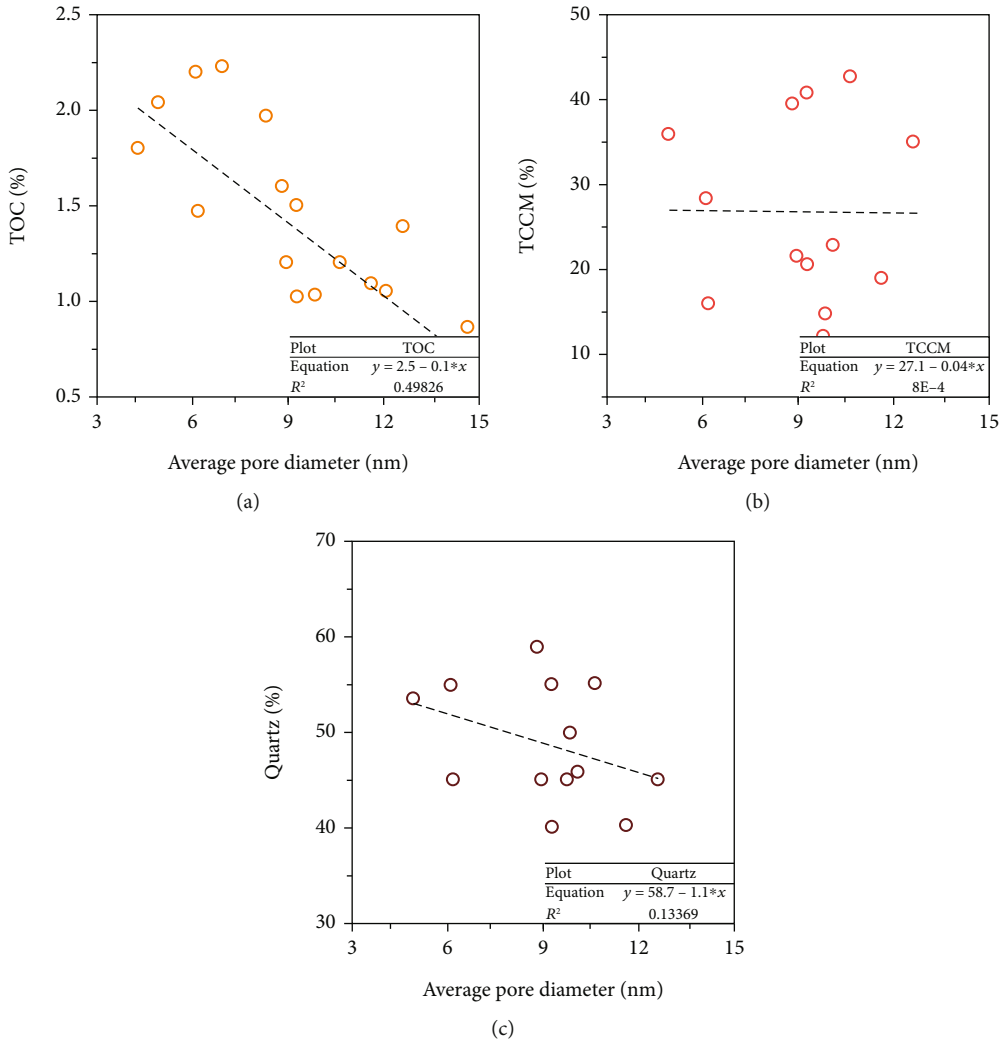

Figure 11: Average pore size correlation analysis.

with TOC (Figure 12(a)). As the thermal evolution of organic matter increases, the intense hydrocarbon generation will lead to volume contraction of organic matter and the formation of organic matter shrinkage joints between the surrounding contact minerals [69]. These shrinkage joints are typically less than 0.5 microns, and the surface of the seam is smooth [70], so the higher the organic matter content, the simpler the pore structure at this scale. Coupled with the role of clay minerals in catalytic hydrocarbon generation, a large number of organic matter-clay complexes were formed [71], and the arrangement of clay minerals is usually relatively regular, which is also the reason for this phenomenon (Figure 12(b)). Micron-level pores are mainly influenced by diagenesis and tectonics, and the correlation with mineral content is not obvious.

The fractal dimensions of mesopores measured by nitrogen and small-angle scattering are significantly lower than that of macropores (Table 3), indicating that the pore morphology of mesopores in shales in the study area is simpler and less heterogeneous than that of microporosity. Which is consistent with the findings of Huang et al. [72] and Xie et al. [73] on the shale pore characteristics of the Longmaxi Formation in the southern Sichuan area and the Taiyuan Formation in the Ordos Basin, the pore surface roughness increases with the increase of pore diameter, the pore structure becomes more and more complex and nonhomogeneous, and the fractal dimension gradually increases. The fractal size D_n measured with nitrogen has a strong positive correlation with TOC (Figure 13(a)), which is opposite to the negative correlation between the fractal dimension and TOC of the macropore part obtained previously. It is related to the development of mesoporous-scale organic matter pores, often with complex internal structures, rough pore surfaces, and diverse internal morphology.

Comparing the fractal dimension of SAXS and LTNA, in the mesoporous range, the unconnected pores are more complex than the accessible pores, and the fractal size lost its correlation with TOC, and the correlation with clay mineral content was enhanced (Figure 13(b)). Illite/smectite mixed layer in clay minerals is mainly attached to the pore

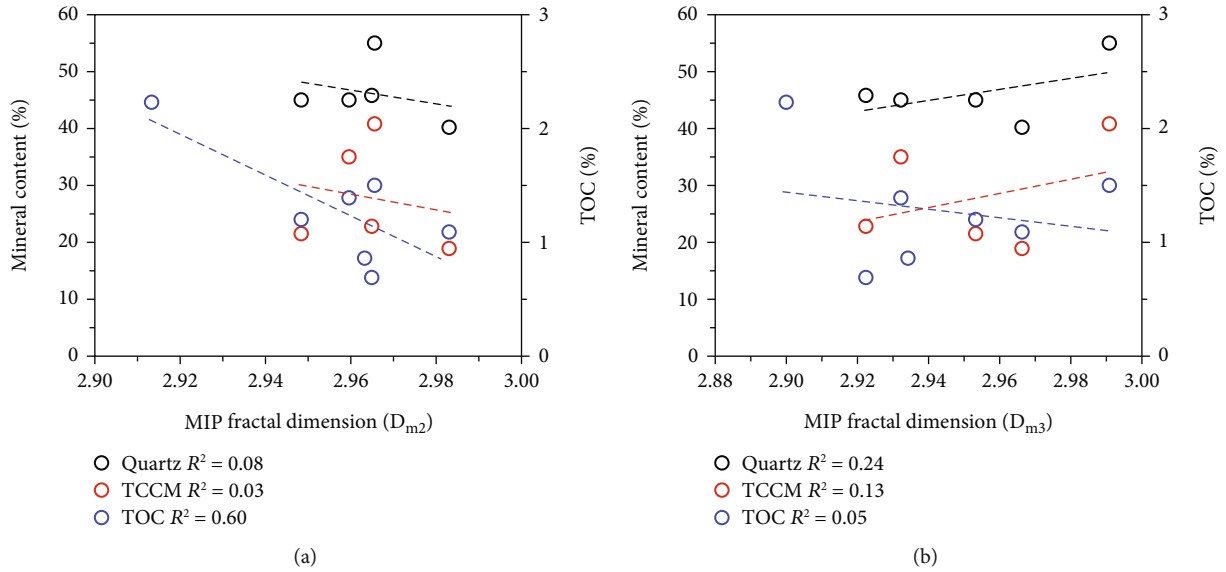

Figure 12: Macropore (MIP) fractal dimension correlation analysis.

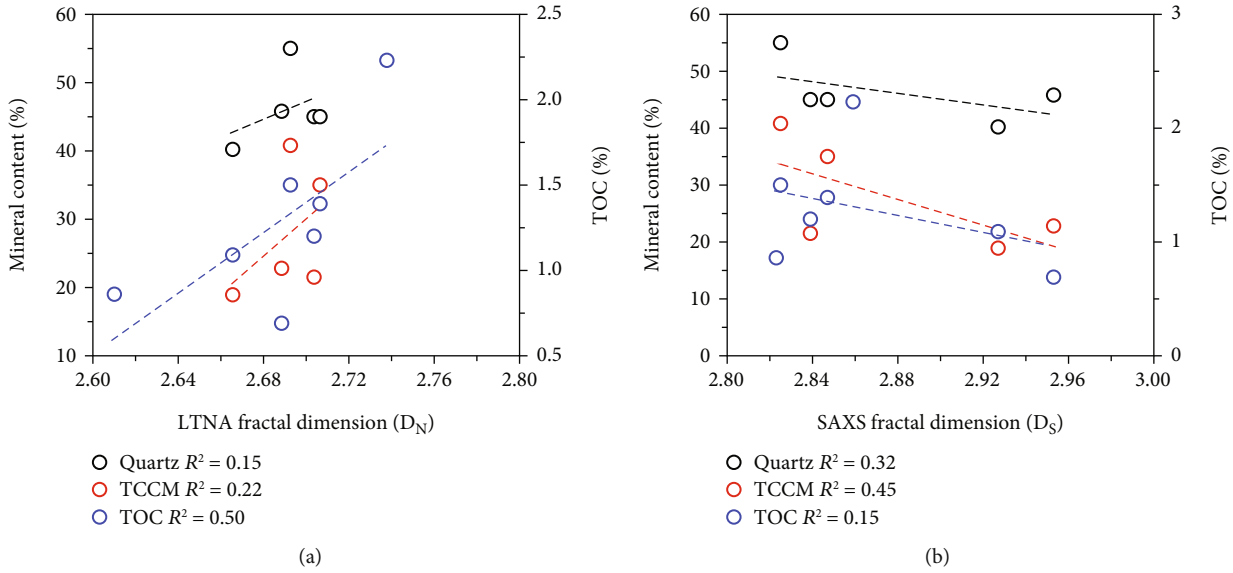

Figure 13: Mesopore (LTNA and SAXS) fractal dimension correlation analysis.

surface and particle surface in a thin film type, which will expand or disperse and transport when encountering water, thus blocking the throat [74, 75]. In addition, the clay minerals are more plastic and susceptible to compaction, resulting in many connected pores being filled [76]. Therefore, the clay minerals become the main controlling factor of the closed pore pores.

6. Conclusion

(1) The pore types of the Luzhai Formation shale in the study area are mainly ink bottle type, parallel plate, and slit-like pores, with large pore throat ratio and poor pore connectivity. The pore-specific surface area of the outcrop samples is dominated by micropores, and the surface area of the core samples is dominated by mesopores. The main controlling factors of the specific surface area include TOC and clay and quartz mineral contents. The pore volume is dominated by mesopores and controlled by clay and quartz mineral contents

(2) The macropore fractal dimension of the shales in the study area is closer to 3 than that of mesopores, with rough, nonhomogeneous pore throat surfaces and complex pore structures. The fractal dimension of mercury injection has a strong negative correlation with TOC for pore sizes from 50 nm to 5 μm, which is mainly related to a large number of organic matter-clay complexes. The micron-level pores are

mainly influenced by diagenesis and tectonics, and the correlation with mineral content is not obvious

(3) In the mesopore range, unconnected pores are overall more complex than accessible pores and correlate well with clays. This is closely related to the fact that clay minerals are susceptible to compaction and cementation during rock formation, which makes original pores compacted, deformed, and blocked, forming a large number of unconnected pores

Data Availability

The data used to support the findings of this study have been made available in the paper.

Conflicts of Interest

The authors declare that there is no conflict of interest regarding the publication of this paper.

Acknowledgments

This research was funded by the National Natural Science Foundation of China (nos. 42130803, 42102183, and 41972139) and the Open Fund of Key Laboratory of Tectonics and Petroleum Resources, Ministry of Education (no. TPR-2020-12).

References

[1] H. K. Nie, Z. L. He, and G. X. Liu, "Status and direction of shale gas exploration and development in China," *Journal of China University of Mining and Technology*, vol. 49, no. 1, pp. 13–35, 2020.

[2] H. K. Nie and J. C. Zhang, "Shale gas accumulation conditions and gas content calculation: a case study of Sichuan Basin and its periphery in the Lower Paleozoic," *Acta Geologica Sinica*, vol. 86, no. 2, pp. 349–361, 2012.

[3] C. N. Zou, Z. Yang, D. Z. Dong, and Q. Zhao, "Formation, distribution and prospect of unconventional hydrocarbons in source rock strata in China," *Earth Science*, vol. 47, no. 5, pp. 1517–1533, 2022.

[4] C. N. Zou, Z. Yang, G. X. Li et al., "Why can China realize the continental "shale oil revolution"," *Journal of Earth Science*, vol. 33, no. 5, pp. 1324–1327, 2022.

[5] D. Z. Dong, S. K. Gao, and J. L. Huang, "A discussion on the shale gas exploration & development prospect in the Sichuan Basin," *Natural Gas Industry*, vol. 34, no. 12, pp. 1–15, 2014.

[6] J. C. Zhang, Z. J. Jin, and M. S. Yuan, "Reservoiring mechanism of shale gas and its distribution," *Natural Gas Industry*, vol. 24, pp. 15–18, 2004.

[7] C. N. Zou, Z. D. Da, and S. J. Wang, "Geological characteristics and resource potential of shale gas in China," *Petroleum Exploration and Development*, vol. 37, no. 6, pp. 641–653, 2010.

[8] Y. Zhang and L. Liu, "Insights into the formation mechanism of low water saturation in Longmaxi shale in the Jiaoshiba area, eastern Sichuan Basin," *Earth Science*, vol. 32, no. 4, pp. 863–871, 2021.

[9] Z. Yang, C. N. Zou, S. T. Wu et al., "Characteristics, types, and prospects of geological sweet sections in giant continental shale oil provinces in China," *Journal of Earth Science*, vol. 33, no. 5, pp. 1260–1277, 2022.

[10] Y. C. Li, "Latest domestic shale gas information and analysis," *China Petro Chemical Industry Observer*, vol. 31, no. 3, pp. 80-81, 2021.

[11] S. Y. Luo, C. S. Wang, and Z. Q. Peng, "Shale gas research of Luzhai formation, low Carboniferous in Guizhong depression," *Geology and Mineral Resources of South China*, vol. 32, no. 2, pp. 180–190, 2016.

[12] L. Huang, Z. Y. Xu, and P. W. Wang, "An analysis of resource potential of Upper Paleozoic shale gas in Guizhong depression," *Geology in China*, vol. 39, no. 2, pp. 497–506, 2012.

[13] X. L. Li, W. Y. Li, and R. H. Wang, "Organic geochemical characteristics of the shales of the lower Carboniferous Luzhai formation in the east of Guizhong depression," *Science Technology and Engineering*, vol. 18, no. 9, pp. 39–45, 2018.

[14] Y. F. Wang, G. Y. Zhai, G. H. Liu et al., "Geological characteristics of shale gas in different strata of marine facies in South China," *Earth Science*, vol. 32, no. 4, pp. 725–741, 2021.

[15] Z. H. Lou, C. J. Shang, and G. S. Yao, "Hydrocarbon preservation conditions in marine strata of the Guizhong depression and its margin," *Acta Petrolei Sinica*, vol. 32, no. 3, pp. 432–441, 2011.

[16] R. F. Pan, X. L. Tang, and J. H. Meng, "Shale gas preservation conditions for the Upper Paleozoic in Guizhong depression," *Oil & Gas Geology*, vol. 35, no. 4, pp. 534–541, 2014.

[17] Y. L. Qin, J. Z. Zhang, and Y. F. Wang, "Discovery of shale gas by Guirongye-1 well within Carboniferous Luzhai formation in Guizhong depression, Guangxi," *Geology in China*, vol. 48, no. 2, pp. 667-668, 2021.

[18] K. Yuan, X. X. Fang, and T. Wen, "Accumulation conditions of Devonian shale gas in well GY 1 in northwestern Central Guangxi depression," *China Petroleum Exploration*, vol. 22, no. 4, pp. 90–97, 2017.

[19] R. Chen, K. Yuan, Z. Y. Zhang, and Q. F. Xu, "Geochemical characteristics of organic-rich shale in the Dawuba formation, western Guizhou province," *Petoleum Geology & Experiment*, vol. 41, no. 1, pp. 10–15, 2019.

[20] C. N. Zou, *Unconventional Oil and Gas Geology*, Geological Press, Beijing, China, 2nd edition, 2013.

[21] Z. X. Jiang, X. L. Tang, and Z. Li, "The whole-aperture pore structure characteristics and its effect on gas content of the Longmaxi formation shale in the southeastern Sichuan Basin," *Earth Science Frontiers*, vol. 23, no. 2, pp. 126–134, 2016.

[22] K. Jiao, S. P. Yao, and H. Wu, "Advances in characterization of pore system of gas shales," *Geological Journal of China Universities*, vol. 20, no. 1, pp. 151–161, 2014.

[23] J. N. Li, *Study on Pore Structure Characterization and Connectivity of Shale Reservoir, [M.S. thesis]*, Nanjing University, Nanjing, China, 2017.

[24] C. R. Clarkson, N. Solano, R. M. Bustin et al., "Pore structure characterization of North American shale gas reservoirs using USANS/SANS, gas adsorption, and mercury intrusion," *Fuel*, vol. 103, no. 4, pp. 606–616, 2013.

[25] R. Y. Wang, Z. Q. Hu, L. Dong, and B. Gao, "Advancement and trends of shale gas reservoir characterization and evaluation," *Oil & Gas Geology*, vol. 42, no. 1, pp. 54–65, 2021.

[26] J. C. Zou, Z. Yang, G. G. Lan, and L. Y. Li, "Contrast of low ranked coal reservoir pore fractal features based on mercury intrusion, cryogenic liquid nitrogen," *Coal Geology of China*, vol. 33, no. 10, pp. 22–30, 2021.

[27] X. C. Li, J. X. Gao, S. Zhang, and Y. Li, "Combined characterization of scanning electron microscopy, pore and crack analysis system, and gas adsorption on pore structure of coal with different volatilization," *Earth Science*, vol. 47, no. 5, pp. 1876–1889, 2022.

[28] X. Wang, R. H. Wang, N. Zhang, and W. P. Cen, "Study on reservoir performance of high-over-mature organic-rich shale in Huanjiang area of central Guangxi depression and its influence on gas bearing property," *Mineral Resources and Geology*, vol. 34, no. 6, pp. 1078–1083, 2020.

[29] J. Y. Tao, B. J. Shen, Z. Q. Hu, and A. Y. Pan, "Pore characteristics and evaluation of shale reservoir in Lower Carboniferous Luzhai formation, northern part of middle Guangxi depression," *Petroleum Reservoir Evaluation and Development*, vol. 12, no. 3, pp. 437–444, 2022.

[30] W. J. Zhu, L. X. Gang, X. Z. Jian, X. Y. Lu, L. Zhao, and L. Y. Wen, "Shale gas accumulation conditions and favorable-zone prediction in Lower Carboniferous Luzhai formation in Donglan area of Nanpanjiang depression, China," *Earth Science*, vol. 46, no. 5, pp. 1814–1828, 2021.

[31] X. N. Cao, Z. X. Jiang, X. Li, and G. Z. Wang, "Pore characteristics of shale reservoirs and their influencing factors-example of the Lower Carboniferous Luzhai formation and Middle Devonian Luofu formation in the Guizhong depression," in *2019 Proceedings of the International Conference on Oil and Gas Field Exploration and Development*, pp. 396–398, Xi'an, 2019.

[32] X. Li, Z. Jiang, S. Jiang et al., "Characteristics of matrix-related pores associated with various lithofacies of marine shales inside of Guizhong Basin, South China," *Journal of Petroleum Science and Engineering*, vol. 185, article 106671, 2020.

[33] F. Wang, Y. Cheng, S. Lu, K. Jin, W. Zhao, and Y. Bai, "Influence of coalification on the pore characteristics of middle-high rank coal," *Energy & Fuels*, vol. 28, no. 9, pp. 5729–5736, 2014.

[34] D. C. Liu, *The Analysis of Tectonic Evolution and Preservation Condition of Oil and Gas in Guizhong Depression, [M.S. thesis]*, China University of Petroleum, Beijing, China, 2009.

[35] H. R. Wang, "Some issues of basic geology in Guangxi," *Southern Land Resources*, vol. 20, no. 3, pp. 20–22, 2004.

[36] G. G. Wu, G. S. Yao, Z. Y. Xu, and Q. X. Guo, "Structural patterns and origin of tectonic reformation in Guizhong depression," *Marine Origin Petroleum Geology*, vol. 14, no. 1, pp. 33–40, 2009.

[37] H. W. Luo, M. C. Hou, Y. Li, and Q. Y. Zhou, "Geochemical characteristics and organic matter enrichment of the Lower section of Luzhai formation in Luzhai area, Guangxi, China," *Journal of Chengdu University of Technology (Science & Technology Edition)*, vol. 46, no. 2, pp. 227–239, 2019.

[38] X. Y. Qu, H. L. Li, F. Q. Yang, and Y. J. Mo, "Application of integrated gravitational, magnetic and electrical geophysical methods to the shale gas geological exploration in southern: a case study of Luzhai, Guizhong depression," *Progress in Geophysics*, vol. 34, no. 3, pp. 1081–1088, 2019.

[39] D. F. Hu, Z. H. Wei, R. B. Liu, and Z. W. Fan, "Development characteristics and shale gas exploration potential of the Lower Carboniferous black shale in the Guizhong depression," *Natural Gas Industry*, vol. 38, no. 10, pp. 28–37, 2018.

[40] D. Q. Jiao, Y. S. Ma, J. Deng, and Q. F. Meng, "The sequence-stratigraphic framework and the evolution of paleogeography for Carboniferous of the Guizhou and Guangxi areas," *Geoscience*, vol. 17, no. 3, pp. 294–302, 2003.

[41] E. W. Washburn, "The dynamics of capillary flow," *Physical Review A*, vol. 17, no. 3, pp. 273–283, 1921.

[42] C. Drummond and J. Israelachvili, "Surface forces and wettability," *Journal of Petroleum Science and Engineering*, vol. 33, no. 1-3, pp. 123–133, 2002.

[43] L. H. Zhang, Z. Deng, M. D. Sun et al., "Characterization of closed pores in Longmaxi shale by synchrotron small-angle X-ray scattering," *Energy & Fuels*, vol. 35, no. 8, pp. 6738–6754, 2021.

[44] L. H. Zhang, M. D. Sun, Q. Lv et al., "Evolution of shale microstructure under in situ heat treatment: synchrotron small-angle X-ray scattering," *Energy & Fuels*, vol. 35, no. 5, pp. 4345–4357, 2021.

[45] S. Y. Wang, R. Hu, D. C. Ren, and X. J. Tong, "Genetic Types and development mechanism of shale pores," *Journal of Shandong University of Science and Technology*, vol. 34, no. 6, pp. 9–15, 2015.

[46] W. T. Zeng, W. L. Ding, J. C. Zhang, and Y. X. Li, "Analyses of the characteristics and main controlling factors for the micro/nanopores in Niutitang shale from China's southeastern Chongqing and northern Guizhou regions," *Earth Science Frontiers*, vol. 26, no. 3, pp. 220–235, 2019.

[47] R. G. Loucks, R. M. Reed, S. C. Ruppel, and U. Hammes, "Spectrum of pore types and networks in mudrocks and a descriptive classification for matrix-related mudrock pores," *AAPG Bulletin*, vol. 96, no. 6, pp. 1071–1098, 2012.

[48] H. Zhang, S. J. Jiao, G. H. Li, and L. Q. Xie, *The Research on Unconventional Oil and Gas Reservoir by Scanning Electronic Microscope*, Geological Press, 2016.

[49] L. C. Zhang, D. S. Xiao, S. F. Lu et al., "Pore development of the Lower Longmaxi shale in the southeastern Sichuan Basin and its adjacent areas: insights from lithofacies identification and organic matter," *Marine and Petroleum Geology*, vol. 122, article 104662, 2020.

[50] W. R. Xie, W. Yang, G. Yang, and Y. F. Yang, "Pore structure features of sandstone reservoirs in the Upper Triassic Xujiahe formation in the central part of Sichuan Basin," *Natural Gas Geoscience*, vol. 21, no. 3, pp. 435–440, 2010.

[51] Z. Z. Ling, S. F. Lu, X. C. Chang, and J. Q. Li, "Micro-pore structure and fractal characteristics of terrestrial shales: a case study of Shahezi formation in Xujiaweizi fault depression," *Coal Geology & Exploration*, vol. 49, no. 1, pp. 151–160, 2021.

[52] K. S. W. Sing, D. H. Everett, R. A. W. Haul et al., "Reporting physisorption data for gas/solid systems with special reference to the determination of surface area and porosity (recommendations 1984)," *Pure and Applied*, vol. 57, no. 4, pp. 603–619, 1985.

[53] Y. P. Cheng and B. Hu, "Main occurrence form of methane in coal: micropore filling," *Journal of China Coal Society*, vol. 46, no. 9, pp. 2933–2948, 2021.

[54] M. Thommes, K. Kaneko, A. V. Neimark et al., "Physisorption of gases, with special reference to the evaluation of surface area and pore size distribution (IUPAC technical report)," *Pure and Applied Chemistry*, vol. 87, no. 9, pp. 1051–1069, 2015.

[55] A. P. Radlinski, M. Mastalerz, A. L. Hinde et al., "Application of SAXS and SANS in evaluation of porosity, pore size distribution and surface area of coal," *International Journal of Coal Geology*, vol. 59, no. 3-4, pp. 245–271, 2004.

[56] X. X. Song, Y. G. Tang, W. Li, and F. G. Zeng, "Pore structure in tectonically deformed coals by small angle X-ray scattering," *Journal of China Coal Society*, vol. 39, no. 4, pp. 719–724, 2014.

[57] M. D. Sun, B. S. Yu, Q. H. Hu et al., "Pore connectivity and tracer migration of typical shales in south China," *Fuel*, vol. 203, pp. 32–46, 2017.

[58] M. Sun, J. Zhao, Z. Pan et al., "Pore characterization of shales: a review of small angle scattering technique," *Journal of Natural Gas Science and Engineering*, vol. 78, article 103294, 2020.

[59] B. B. Mandelbrot, J. A. Wheeler, and M. Baron, "The fractal geometry of nature," *Journal de Physique*, vol. 51, no. 3, pp. 286-287, 1983.

[60] Z. H. Xu, M. J. Zheng, Z. H. Liu, and J. X. Deng, "Petrophysical properties of deep Longmaxi formation shales in the southern Sichuan Basin, SW China," *Petroleum Exploration and Development*, vol. 47, no. 6, pp. 1100–1110, 2020.

[61] H. J. Fu, D. T. Yan, C. P. Yao et al., "Pore structure and multi-scale fractal characteristics of adsorbed pores in marine shale: a case study of the Lower Silurian Longmaxi shale in the Sichuan Basin, China," *Journal of Earth Science*, vol. 33, no. 5, pp. 1278–1290, 2022.

[62] Y. T. Gu, X. X. Li, Q. Wang, and S. G. Yang, "On the different characteristics of organic pores in shale and their influencing factors: taking typical marine, continental, and transitional facies reservoirs in China as examples," *Acta Sedimentologica Sinica*, vol. 39, no. 4, pp. 794–810, 2021.

[63] X. Tang, Z. Jiang, Z. Li et al., "The effect of the variation in material composition on the heterogeneous pore structure of high-maturity shale of the Silurian Longmaxi formation in the southeastern Sichuan Basin, China," *Journal of Natural Gas Science and Engineering*, vol. 23, pp. 464–473, 2015.

[64] Z. W. Li, Z. Y. Hao, Y. Pang, and Y. B. Gao, "Fractal dimensions of coal and their influence on methane adsorption," *Journal of China Coal Society*, vol. 40, no. 4, pp. 863–869, 2015.

[65] L. S. Gen, S. Y. Wang, W. Sun, and B. Ran, "Characteristics of black shale in Wufeng formation and Longmaxi formation in Sichuan Basin and its peripheral areas," *Journal of Chengdu University of Technology*, vol. 40, no. 6, pp. 621–639, 2013.

[66] Z. X. Jiang, X. Li, X. M. Li, and Z. G. Yuan, "Characteristic differences and controlling factors of pores in typical South China shale," *Oil and Gas Geology*, vol. 42, no. 1, pp. 41–53, 2021.

[67] W. Zhang, B. Huang, X. Yu, and J. Zhang, "Interpretation of BJH method for calculating aperture distribution process," *Chem*, vol. 35, no. 2, pp. 98–106, 2020.

[68] H. D. Bale and P. W. Schmidt, "Small-angle X-ray-scattering investigation of submicroscopic porosity with fractal properties," *Physical Review Letters*, vol. 53, no. 6, pp. 596–599, 1984.

[69] Q. L. Xiao, A. Liu, C. X. Li, and Q. Cheng, "Formation and evolution of nanopores in highly matured shales at over mature stage: insights from the hydrous pyrolysis experiments on Cambrain Shuijintuo shale from the middle Yangtze region," *Earth Science*, vol. 45, no. 6, pp. 2160–2171, 2020.

[70] Y. Chen, Q. H. Hu, J. H. Zhao, M. M. Meng, and N. Yi, "Lamina characteristics and their influence on reservoir property of lacustrine organic-rich shale in the Dongying Sag, Bohai Bay Basin," *Oil and Gas Geology*, vol. 43, no. 2, pp. 307–324, 2022.

[71] J. G. Cai, Y. J. Bao, S. Y. Yang, X. X. Wang, and D. D. Fan, "Study of organic matter preservation and enrichment mechanisms in muddy sediments and mudstones," *The 3rd National Sedimentology Congress*, vol. 41, p. 2, 2004.

[72] K. Z. Huang, S. F. Lu, J. J. Li, and Y. W. Ju, "Marine shale of Longmaxi formation, Nanchuan area, Sichuan Basin mineral formation and microscopic pore structure characteristics," in *Proceedings of the Ninth National Congress of the Chinese Society of Mineral and Rock Geochemistry and the 16th Annual Academic Conference*, p. 2, Beijing, 2017.

[73] W. D. Xie, M. Wang, H. Wang, and D. H. Yue, "Multi-scale fractal characteristics of pores in transitional shale gas reservoir," *Natural Gas Geoscience*, vol. 33, no. 3, pp. 451–460, 2022.

[74] Q. Liu, P. Li, Z. Jin et al., "Organic-rich formation and hydrocarbon enrichment of lacustrine shale strata: a case study of Chang 7 member," *Science China Earth Sciences*, vol. 65, no. 1, pp. 118–138, 2022.

[75] S. Stricker, S. J. Jones, N. Meadows, L. Bowen, and L. Bai, "Reservoir quality of fluvial sandstone reservoirs in salt-walled mini-basins: an example from the Seagull field, Central Graben, North Sea, UK," *Petroleum Science*, vol. 15, no. 1, pp. 1–27, 2018.

[76] L. Shi, Z. Jin, W. Yan, X. Zhu, X. Xu, and B. Peng, "Influences of overpressure on reservoir compaction and cementation: a case from northwestern subsag, Bozhong sag, Bohai Bay Basin, East China," *Petroleum Exploration and Development*, vol. 42, no. 3, pp. 339–347, 2015.